RSC Advances




ROYAL SOCIETY OF CHEMISTRY

www.rsc.org/advances

Journal Name RSC Advances Dynamic Article Links ►

Cite this: DOI: 10.1039/c0xx00000x

www.rsc.org/xxxxxx

ARTICLE TYPE

# Nanosheet-Assembled 3D Nanoflowers of Ruthenium Oxide with Superior Rate Performance for Supercapacitor Applications

**Ji-Young Kim,[a] Kwang-Heon Kim,[a] Hyun-Kyung Kim,[a] Sang-Hoon Park,[a] Kyung Yoon Chung[b] and Kwang-Bum Kim*[a]**

**Received (in XXX, XXX) Xth XXXXXXXXX 20XX, Accepted Xth XXXXXXXXX 20XX**
**DOI: 10.1039/b000000x**

Nanosheet-assembled 3D nanoflowers of ruthenium oxide were prepared by a microwave-hydrothermal process without using a template. The 3D nanoflowers consisted of interconnected spheres and had sizes of 250–300 nm. The mechanism of formation of the nanosheet-assembled 3D nanoflowers was determined on the basis of experimental evidence. The specific capacitance of an electrode based on these 3D nanoflowers was calculated and found to be 545.2 F $g^{-1}$ at a discharging current density of 0.5 A $g^{-1}$. The unique morphology of the nanoflowers allows $H^+$ ions greater electrochemical access to the pores of the active $RuO_2$ matrix, leading to a high specific capacitance. Moreover, the specific capacitance of the electrode decreased by only 8.6% (from 545.2 to 498.2 F $g^{-1}$) as the discharging current density was increased from 0.5 to 50 A $g^{-1}$, indicating its excellent rate capability. This superior rate capability could also be attributed to the porous nature of the nanoflowers. The excellent electrochemical properties of the 3D nanoflowers make them an attractive material for use in electrochemical capacitors.

## Introduction

The synthesis of nanostructured materials with a well-defined morphology is important for improving their performance in applications such as heterogeneous catalysis, sensory devices, and energy storage devices.[1] Among the various energy storage devices available, electrochemical capacitors (or supercapacitors) have gained considerable attention owing to their high power density, high charging and discharging rates, and long cycle life.[2-5]

These supercapacitors store energy either capacitively or pseudocapacitively.[6] The capacitive process is based on non-Faradaic charge separation at the electrode/solution interface, whereas the pseudocapacitive process consists of Faradaic redox reactions occurring within active electrodes. Typical materials used for making pseudocapacitive electrodes include conducting polymers and transition metal oxides.[7-13]

The presence of nanosized active materials can enhance the redox reactions and electrochemical utilization of the electroactive materials because nanosized materials provide a short diffusion path. In particular, 3D hierarchical structures constructed using low-dimensionality nanoscale building blocks, such as 1D nanorods and 2D nanosheets, have attracted significant attention in recent years. The synthesis of nanostructured materials from 2D nanosheets has become an important strategy for enhancing the electrochemical performance of supercapacitor electrodes.[14] Next-generation high-performance supercapacitors are being developed for realizing ultrathin nanostructures (thickness < 10 nm).[15] Furthermore, 3D hierarchical nanostructures assembled from 2D ultrathin nanosheets provide the electrolyte greater access to the active surface of the electrode, enhancing its rate capability.

A number of research groups have reported hierarchical architectures based on transition metal oxides such as iron oxides, $MnO_2$, $V_2O_5$, $TiO_2$, and $SnO_2$.[14-19] However, 3D ruthenium oxide nanostructures assembled using 2D nanosheets have not been reported. Ruthenium oxide ($RuO_2 \cdot xH_2O$) can exist in an amorphous or a crystalline form. It is one of the most promising electrode materials for aqueous electrochemical capacitors because of its high specific capacitance and high rate capability. Most ruthenium oxide structures used in capacitors are 0D nanostructures (nanoparticles) prepared by sol-gel or hydrothermal methods.[20] Owing to their large specific surface area and high surface energy, ruthenium oxide nanoparticles tend to agglomerate to minimize their surface energy. Hybridization of the nanoparticles with carbon can prevent their agglomeration, thereby enhancing their electrochemical properties.[21] However, the capacitance of the resulting composite electrodes is low because carbon has a low specific capacitance.[13] Therefore, only ruthenium oxide is used as the active electrode material to shorten the diffusion path in the electrode.

Herein, we report the microwave-hydrothermal synthesis of a novel ruthenium oxide nanostructure—nanosheet-assembled 3D nanoflowers—without using a template. Electrodes prepared from the nanoflowers exhibited high specific capacitance and superior rate capability, making them attractive candidates for use in electrochemical capacitors. Metal oxide electrodes having high specific capacitances at a current density as high as 200 A $g^{-1}$

have not yet been reported. These significant improvements in capacitance and rate capability result from the 3D porous structure of the electrode since the porous nature provides the electrolyte greater access to the electrode's active surface. Moreover, a mechanism for the formation and morphological evolution of the nanoflowers is proposed.

## Experimental section

## Experimental Section

### Synthesis

The nanoflowers were synthesized by a microwave-hydrothermal process. Typically, 0.1 g of $RuCl_3 \cdot nH_2O$ (Sigma-Aldrich) powder was added to 100 mL of a 10 M NaOH aqueous solution (Sigma-Aldrich), and the solution was stirred for 3 days. Then, the resulting green solution, which contained the black precipitate, was loaded into a Teflon vessel. The vessel was sealed and placed in a microwave system (MARS-5, CEM). The mixtures were heated to 200 ℃ in less than 10 min and maintained at 200 ℃ for 10, 30, 60, or 240 min. After the reaction was completed, the Teflon vessel was taken out of the microwave system and cooled with tap water. The resulting suspension was filtered, and the residue was washed with water and dried in a freeze dryer.

### Characterization

The structure and morphology of the products were characterized by XRD analyses (Rigaku, CuKα, 40 kV, 20 mA), TEM (JEM-3010, JEOL) and Raman spectroscopy (T64000, Jobin Yvon). XPS (Thermo Electron, ESCA 2000) was used for the elemental analysis of the products. Thermal data for the products were obtained from thermogravimetric analyses (Mettler Toledo), which were performed in flowing air by increasing the temperature from room temperature to 800 ℃ at the rate of 10 ℃ $min^{-1}$.

The electrochemical measurements were performed using a three-electrode electrochemical cell. A platinum plate and a saturated calomel electrode were used as the counter and reference electrodes, respectively. The working electrode was fabricated using a mix of 75 wt% nanoflowers, 15 wt% carbon black, and 10 wt% polyvinylidene fluoride dissolved in N-methylpyrrolidone. The slurry was coated onto a titanium foil and dried overnight at 80 ℃. The area of the working electrode was 1 × 1 $cm^2$, and it contained approximately 1–2 mg of the nanoflowers.

Cyclic voltammetry and the charge/discharge tests were performed using a potentiostat/galvanostat (Princeton Applied Research VMP3) and a 1 M $H_2SO_4$ solution in a 0.0–1.0 $V_{SCE}$ potential window. The current response in the CV curves was normalized with respect to the mass of the nanoflowers.

## Results and discussion

The most common oxidation number of ruthenium in ruthenium compounds (*e.g.*, fluorides, chlorides, and oxides of ruthenium) is +4.[22] According to the potential-pH diagram, orange-collared ruthenate ($RuO_4^{2-}$; oxidation number: +6) is stable at room temperature in highly alkaline aqueous solutions free from reducing agents.[22] When the pH is lowered to 12, $RuO_4^{2-}$ tends to decompose via the disproportionation reaction of ruthenate, $RuO_4^{-2}$, shown below, yielding black-collared $RuO_2 \cdot 2H_2O$ and green-collared perruthenate ($RuO_4^-$) anions.[2,23]

$$3\,RuO_4^{2-} + (2+x)H_2O \rightarrow 2RuO_4^- + RuO_2 \cdot xH_2O + 4OH^- \quad (1)$$

Immediately after the addition of $RuCl_3 \cdot nH_2O$ to 10 M NaOH, the solution turned green and a black precipitate was formed in a small amount (Figure S1). The disproportionation reaction of $RuO_4^{2-}$ suggested that this precipitate was formed by $RuO_2 \cdot 2H_2O$. According to the potential-pH diagram, the green supernatant likely contained green-collared $RuO_4^-$ anions. The obtained precipitate was analyzed by X-ray photoelectron spectroscopy (XPS), and the results confirmed the presence of $RuO_2$ (Figure S2a).

The nanoflowers were prepared by a microwave-hydrothermal treatment of the green-collared solution containing the black precipitate at 200 ℃ for 240 min (Figure 1). Before the treatment, the initially formed black precipitate consisted mainly of irregularly agglomerated ruthenium oxide particles with diameters of 300–400 nm (Figures S2b and S2c). After 240 min of microwave irradiation, flower-like interconnected spherical ruthenium oxide particles with sizes of 250–300 nm were observed (Figure 1a). Most interestingly, the hierarchical porous structures of these nanoflowers were formed of single nanosheets. A magnified TEM image (Figure 1c) shows the detailed morphology of the nanoflowers, which were composed of nanosheets ~2–3 nm in thickness. **A scanning electron microscope (SEM) images further reveal the morphology of the nanoflowers, which are composed of nanosheets with a 3D porous structure. (Figures S3)**

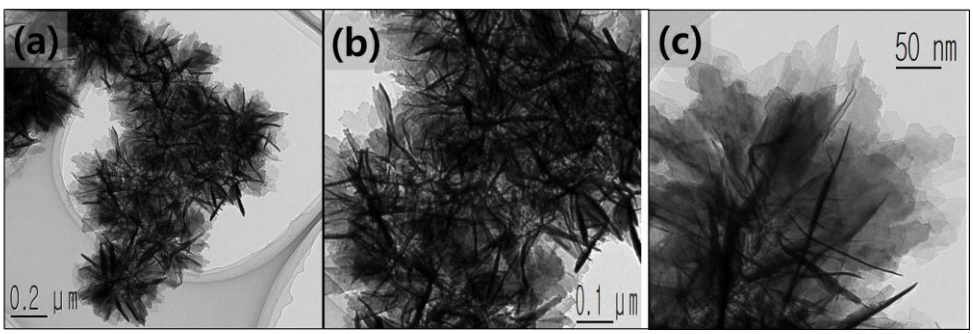


**Fig. 1** TEM images of 3D ruthenium oxide nanoflowers assembled using nanosheets. (b) and (c) are magnified images of (a).

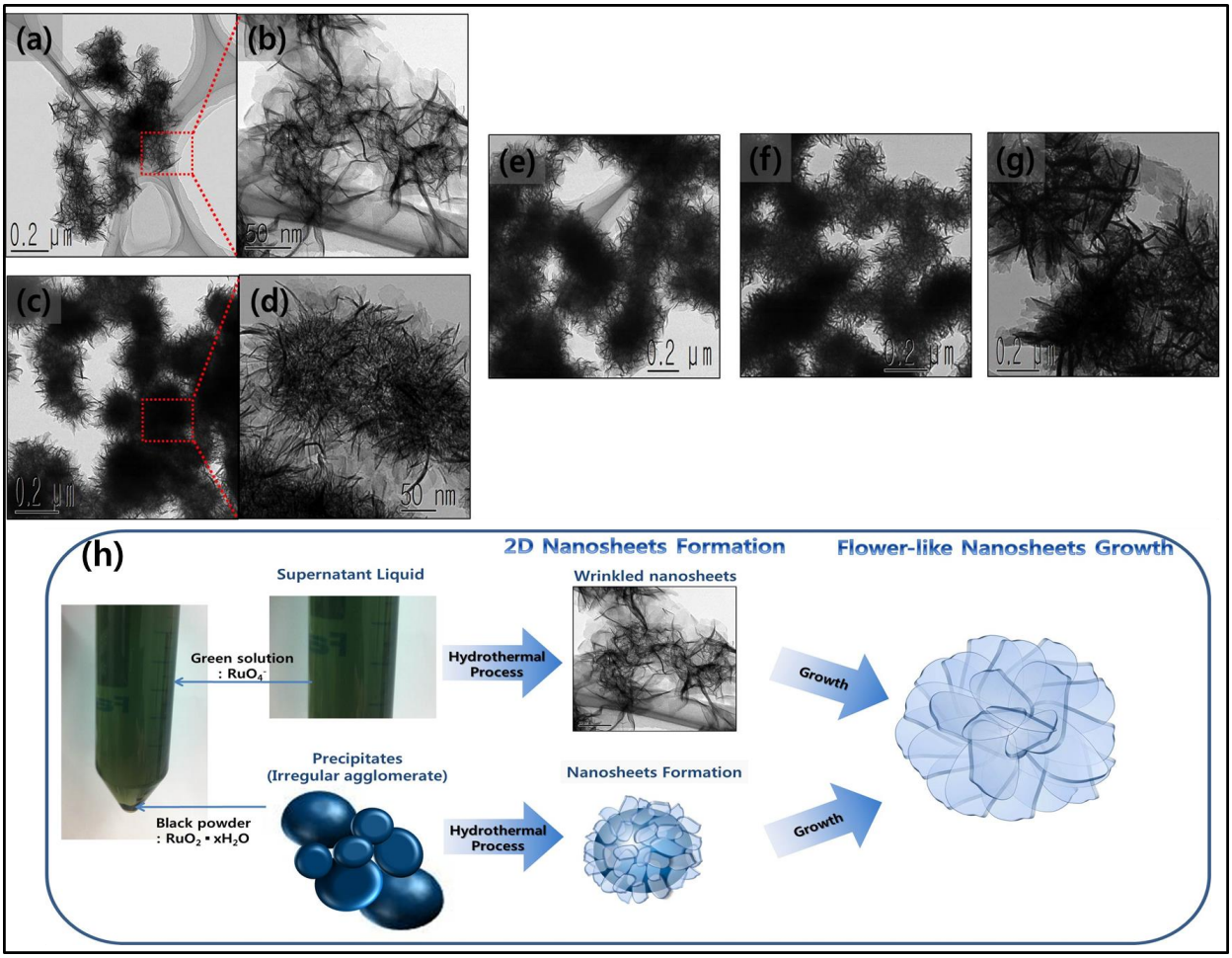


**Fig.2** TEM images of the 3D nanoflowers formed for different reaction times: (a) wrinkled nanosheets observed after 10 min. (c) particles covered with nanosheets observed after 10 min. (b) and (d) are magnified images of (a) and (c), respectively. (e–g) Morphology of the nanoflowers observed after 30, 60, and 240 min, respectively. (h) Scheme illustrating proposed mechanism for nanoflower formation from different states of ruthenium.

To investigate the formation mechanism of the nanoflowers, we analyzed the changes in the structure and morphology of the intermediates formed at different reaction times (10–240 min). Figures 2a–g show TEM images of the nanoflowers formed for different reaction times. After 10 min, nanostructures with two kinds of morphologies were observed: *wrinkled nanosheets* (Figures 2a and b) and *particles composed of nanosheets* (Figures 2c and d). We propose that the wrinkled nanosheets were formed from $RuO_4^-$ anions. Moreover, the nanosheets were generated on the surfaces of irregular particles during the initial stage of the hydrothermal process. Ruthenium dioxide in its hydrated form ($RuO_2 \cdot xH_2O$) is soluble at elevated pH (>13).[24]

$$RuO_2 \cdot xH_2O + 4OH^- = RuO_4^{2-} + (2+x)H_2O + 2e^- \quad (2)$$

In addition, the high temperature and pressure of the closed reaction vessel aided the dissolution reaction. After 30 min, no solid particles remained and the product was composed entirely of nanoflowers. This was due to the growth of the wrinkled nanosheets and formation of nanosheets on solid particles (Figure 2e). When the reaction time was increased to 240 min, the size of the nanoflowers increased from 100 to over 400 nm, while their spherical shape was maintained (Figures 2f and 2g). Figure 2g shows that the nanoflowers were uniform in appearance and were composed of numerous nanosheets radiating from the centre. These interconnected, ultrathin nanosheets were widely spaced, which allowed for easier transport of the electrolyte ions. [25]

On the basis of the TEM results and analysis, we propose two mechanisms for the morphological evolution of the nanoflowers (Figure 2h). Before the hydrothermal treatment, irregular agglomerates of ruthenium oxide particles are generated through $RuO_4^{2-}$ disproportionation. The reduction of $RuO_4^-$ to $RuO_2$ results in the formation of wrinkled nanosheets in the supernatant. The presence of $RuO_2$ precipitates suggests that the nanosheets are formed by a dissolution–recrystallization mechanism. The surfaces of the $RuO_2$ precipitates dissolve in the $RuO_4^-$ solution, and nanosheets are formed by recrystallization in the aqueous alkaline solution at high temperatures during the hydrothermal process. Therefore, the nanoflowers are formed by the assembly of ultrathin nanosheets, whose size increases gradually. The unique morphology of the nanoflowers provides $H^+$ ions better electrochemical access to the pores of the active $RuO_2$ matrix, leading to a high specific capacitance. The porous nature of the nanoflowers allows fast ion diffusion into their $RuO_2$ core.

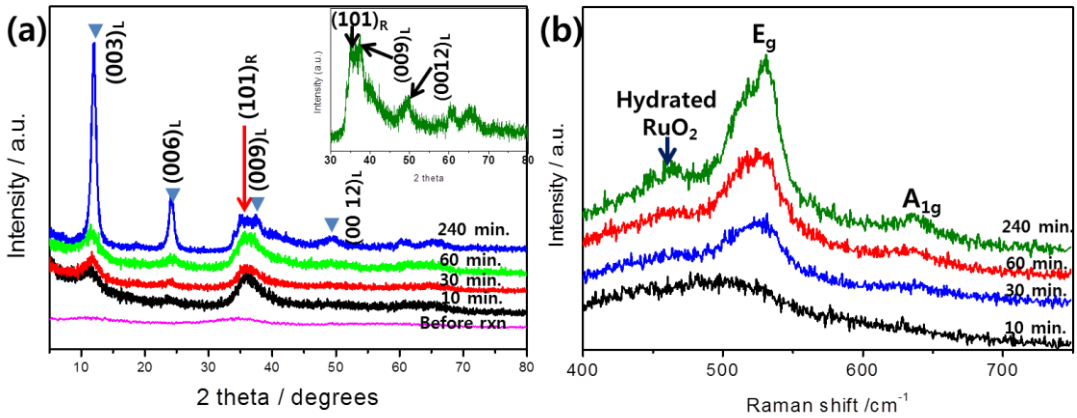


**Fig.3** (a) XRD patterns and (b) Raman spectra of the nanoflowers formed for different reaction times. Inset shows the magnified XRD pattern for the nanoflowers formed after 240 min. (L: Layered structure, R: Rutile structure).

Figure 3a shows variations in the X-ray diffraction (XRD) patterns of the nanoflowers formed for different reaction times. The pattern for the black precipitate (before the reaction) does not reveal any peaks, indicating that the precipitate was amorphous. After 10 min of treatment, two broad peaks were observed, at $2\theta$ = 12° and 37°. These peaks could be indexed as the $(101)_R$ and $(003)_L$ reflections of rutile $RuO_2$ (JCPDS No. 43-1027) and the layered structure, respectively. The peak intensity of the $(101)_R$ reflection did not change significantly with increases in the reaction time. In contrast, the $(003)_L$ peak became sharper with the increase, indicating that the layered structure became predominant with time. After 240 min, a number of diffraction peaks were observed; these could be indexed as the $(003)_L$, $(006)_L$, $(009)_L$, and $(00\ 12)_L$ reflections of the layered structure since a series of (00*l*) diffraction peaks are typical of a well-ordered layered structure. The inset in Figure 3a shows the magnified XRD pattern of the nanoflowers formed after 240 min. This pattern reveals the crystallographic structure of the nanoflowers to be a mixture of the rutile and layered phases.

The nanoflowers were subjected to Raman spectroscopy so as to examine the changes in their microstructure with the increase in reaction time. For all the reaction times studied, the spectra showed a broad peak at 470 $cm^{-1}$ (Figure 3b); this was attributable to hydrated $RuO_2$.[26-28] The intensities of all the Raman peaks increased with the increase in reaction time. The major Raman peaks—attributable to the $E_g$ and $A_{1g}$ modes of rutile $RuO_2$ crystals—were located at 525 and 646 $cm^{-1}$, respectively. Ruthenium oxide nanosheets with a rutile structure could be prepared in over 30 min by microwave-hydrothermal process. The crystallinity of the nanosheets increased with the reaction time. The presence of $RuO_2$ was also confirmed by the XPS-based measurements (Figures S4). XPS was also employed to determine the composition of the nanoflowers. Peaks corresponding to Ru $3d_{5/2}$, Ru $3d_{3/2}$, and O1s appeared at 281.2 eV, 285.4 eV, and 530.0 eV, respectively. These corresponded to the binding energy of $Ru^{4+}$ and suggested the presence of $RuO_2$.[29, 30]

The electrochemical properties of ruthenium oxide are highly dependent on its degree of hydration.[20] Thermogravimetric analysis was performed in order to estimate the hydration number (x) of $RuO_2 \cdot xH_2O$ present in the nanoflowers formed for a reaction time of 240 min. The nanoflowers showed a continuous loss in weight up to 200 ℃. The TGA data suggested that the nanoflowers had lost approximately 15% of their initial weight (Figure S5). On the basis of the TGA data, the chemical composition of the as-prepared $RuO_2 \cdot xH_2O$ was determined to be $RuO_2 \cdot 1.56H_2O$.[31]

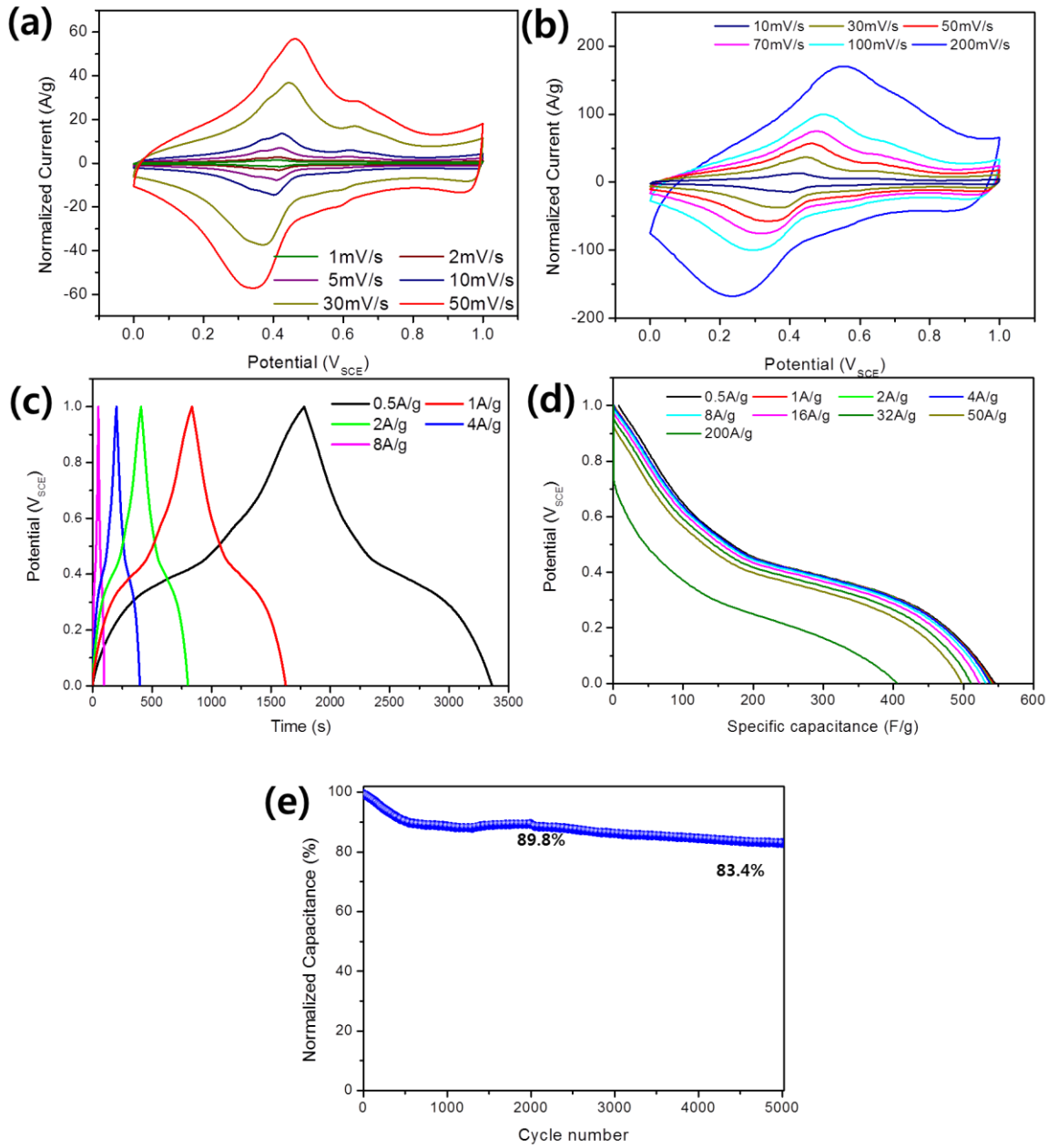


**Fig.4** (a) Cyclic voltammograms (CVs) at scan rates of 1–50 mV $s^{-1}$ (b) CVs at scan rates of 10–200 mV $s^{-1}$ (**c) Charge-discharge curves (current density:0.5~8 A $g^{-1}$) (d) Discharge curves (current density:0.5~200 A $g^{-1}$) and (e) Cycling performance of the nanoflower electrode**.

Cyclic voltammetry and charge/discharge tests were performed to evaluate the electrochemical properties of an electrode based on the synthesized nanoflowers. Cyclic voltammograms (CVs) of the electrode were measured in the 0.0–1.0 $V_{SCE}$ potential window at different scan rates in an aqueous 1 M $H_2SO_4$ solution to evaluate the electrode's rate capability. The current in the CV curves (Figures 4a and 4b) was normalized with respect to the electrode mass. The shapes of the CV curves revealed that the charge storage mechanism was very different from that of an electric double-layer capacitor, which normally displays a nearly rectangular shape. The redox peaks observed during the anodic and cathodic scans at different scan rates confirmed the redox behaviour of the electrode. At a low scan rate, the electrode showed a strong peak at 0.40 V and two broad peaks, at 0.32 and 0.60 V, respectively (Figure S6). The clear redox peaks indicated that the capacitance results mainly from the Faradaic mechanism, with there being a contribution from the double layer mechanism as well. It is assumed that the ruthenium ions in the bulk react with protons. The electrode exhibited a featureless CV for scan rates as high as 200 mV $s^{-1}$, indicating its superior high rate capability, which was because the electrolyte had greater access to the electrode's active surface.

Charge-discharge tests were performed at different current densities (0.5–200 A $g^{-1}$) **(Figure 4c and d).** For densities

between 0.5–50 A $g^{-1}$, no significant voltage (IR) drop was observed at the beginning of the discharge cycle; **this suggests that the crystallinity of the nanoflower electrode was reasonably high.** The specific capacitance of the electrode was calculated to be 545.2, 538.0, 531.9, 523.1, and 498.2 F $g^{-1}$ at discharging current densities of 0.5, 4, 8, 16, and 50 A $g^{-1}$, respectively, indicating a decrease of only 8.6% in the specific capacitance over the investigated discharging current density.

Surprisingly, the specific capacitance of the electrode was 405.9 F $g^{-1}$ at a current density of 200 A $g^{-1}$. An extremely fast charge-discharge protocol was used to demonstrate the excellent rate capability of the electrode. **The superior rate capability of nanoflower ruthenium oxide electrode is attributed to unique morphology-assembly of untrathin nanosheets.** The increase in specific capacitance can be explained by the formation of a more open framework in the nanoflowers; this aids electrochemical charge storage. The electrode showed a specific capacitance of 545.2 F $g^{-1}$, owing to its diffuse structure and large porous area (surface area of 97 $m^2$ $g^{-1}$, Figure S7). Some factors that likely contribute to the higher specific capacitance of the nanoflowers are easy access to the interiors of their pores and fast mass transport of $H^+$ ions to electrochemically active sites.

For an electrochemical capacitor to have high practical applicability, it must have high cyclability. Figure 4d shows the variations in the specific capacitance of the nanoflower electrode for different cycles at a constant scan rate of 50 mV $s^{-1}$. Even after 2000 and 5000 cycles, the specific capacitance was maintained at 89.8 and 83.4 % of the initial value, respectively. Hydrous forms of ruthenium oxide prepared by sol-gel processes have been shown to exhibit a high specific capacitance of 720 F $g^{-1}$ at a scan rate of 2 mV $s^{-1}$.[32] However, the specific capacitance of these forms when measured at a scan rate of 50 mV $s^{-1}$ was only about 36% of that measured at 2 mV $s^{-1}$. Moreover, the capacitance of highly hydrous $RuO_2$ (hydration degree x = 2.0) dropped so rapidly that only 4% of its initial capacitance was maintained after 50 cycles. Even though the cyclability of hydrous $RuO_2$ (hydration degree x = 0.5) improves after being heated at 150 ℃, the loss in its capacitance is still significant (45% after 200 cycles). [12]

The superior cycling stability and excellent kinetics of the 3D ruthenium oxide (hydration degree x = 1.5) nanoflowers-based electrode suggest that a well-crystallized layered phase can be achieved by microwave-hydrothermal treatment. The unique morphology of the nanoflowers gives rise to the remarkable rate capability and superior cycle performance of the electrode.

## Conclusions

We successfully synthesized novel ruthenium oxide nanostructures—nanosheet-assembled 3D nanoflowers—via a microwave-hydrothermal process. These nanoflowers consisted of interconnected spheres and had sizes of 250–300 nm. Moreover, they exhibited excellent electrochemical performance owing to their high specific area and high crystallinity. A decrease of only 8.6% was noticed in the specific capacitance (from 545.2 to 498.2 F $g^{-1}$) when the discharging current density was increased from 0.5 to 50 A $g^{-1}$. This was indicative of their excellent rate capability. The significant improvements in capacitance and excellent kinetics result from the hierarchical 3D porous nature of the nanoflowers, allowing the electrolyte greater access to the active surface of the electrode.

## Acknowledgements

## Notes and references

[a] *Department of Materials Science and Engineering, Yonsei University 134 Shinchon-dong, Seodaemoon-gu, Seoul 120-749, Republic of Korea. Fax: 82-2-312-5375; Tel: 82-2-365-7745; E-mail: kbkim@yonsei.ac.kr*
[b] *Center for Energy Convergence, Korea Institute of Science and Technology, Hwarangno 14-gil 5, Seongbuk-gu, Seoul 136-791, Republic of Korea.*

† Electronic Supplementary Information (ESI) available: The image of the NaOH aqueous solution after addition of $RuCl_3 \cdot nH_2O$, properties of the initial precipitates before being subjected to the microwave-hydrothermal reaction, XPS spectra and TGA of 3D ruthenium oxide nanoflowers and results of CV of the ruthenium oxide nanoflowers-based electrode]. See DOI: 10.1039/b000000x/

1. G. R. Li, H. Xu, X. F. Lu, J. X. Feng, Y. X. Tong and C. Y. Su, *Nanoscale*, 2013, **5**, 4056-4069.
2. W. T. Deng, X. B. Ji, Q. Y. Chen and C. E. Banks, *Rsc Advances*, 2011, **1**, 1171-1178.
3. Y. Hou, Y. W. Cheng, T. Hobson and J. Liu, *Nano Letters*, 2010, **10**, 2727-2733.
4. G. H. Yuan, Z. H. Jiang, A. Aramata and Y. Z. Gao, *Carbon*, 2005, **43**, 2913-2917.
5. S. Liu, S. Sun and X.-Z. You, *Nanoscale*, 2014, **xx**, xxx.
6. B. E. Conway, *Electrochemical supercapacitors: scientific fundamentals and technological applications*, Springer, 1999.
7. E. Frackowiak and F. Beguin, *Carbon*, 2001, **39**, 937-950.
8. Y. G. Wang, H. Q. Li and Y. Y. Xia, *Advanced Materials*, 2006, **18**, 2619-2623.
9. M. Toupin, T. Brousse and D. Belanger, *Chemistry of Materials*, 2004, **16**, 3184-3190.
10. W. Sugimoto, H. Iwata, Y. Yasunaga, Y. Murakami and Y. Takasu, *Angewandte Chemie-International Edition*, 2003, **42**, 4092-4096.

11. C. C. Hu, K. H. Chang, M. C. Lin and Y. T. Wu, *Nano Letters*, 2006, **6**, 2690-2695.
12. J. H. Jang, A. Kato, K. Machida and K. Naoi, *Journal of the Electrochemical Society*, 2006, **153**, A321-A328.
13. J. Y. Kim, K. H. Kim, S. H. Park and K. B. Kim, *Electrochimica Acta*, 2010, **55**, 8056-8061.
14. R. Z. Ma and T. Sasaki, *Advanced Materials*, 2010, **22**, 5082-5104.
15. H. Jiang, T. Sun, C. Z. Li and J. Ma, *Journal of Materials Chemistry*, 2012, **22**, 2751-2756.
16. Z. Y. Weng, H. Guo, X. M. Liu, S. L. Wu, K. W. K. Yeung and P. K. Chu, *Rsc Advances*, 2013, **3**, 24758-24775.
17. Y. L. Li, J. J. Wang, Y. Zhang, M. N. Banis, J. Liu, D. S. Geng, R. Y. Li and X. L. Sun, *Journal of Colloid and Interface Science*, 2012, **369**, 123-128.
18. C. Wang, Y. Zhou, M. Y. Ge, X. B. Xu, Z. L. Zhang and J. Z. Jiang, *Journal of the American Chemical Society*, 2010, **132**, 46-47.
19. Q. Chen, W. Z. Zhou, G. H. Du and L. M. Peng, *Advanced Materials*, 2002, **14**, 1208-1211.
20. J. P. Zheng, P. J. Cygan and T. R. Jow, *Journal of the Electrochemical Society*, 1995, **142**, 2699-2703.
21. J. Y. Kim, K. H. Kim, S. B. Yoon, H. K. Kim, S. H. Park and K. B. Kim, *Nanoscale*, 2013, **5**, 6804-6811.
22. M. Pourbaix, *M. Pourbaix, published 1974 by NACE, 644*, 1974.
23. R. E. Connick and C. R. Hurley, *Journal of the American Chemical Society*, 1952, **74**, 5012-5015.
24. T. P. Luxton, M. J. Eick and K. G. Scheckel, *Journal of Colloid and Interface Science*, 2011, **359**, 30-39.
25. H. Jiang, C. Z. Li, T. Sun and J. Ma, *Nanoscale*, 2012, **4**, 807-812.
26. S. Bhaskar, P. S. Dobal, S. B. Majumder and R. S. Katiyar, *Journal of Applied Physics*, 2001, **89**, 2987-2992.
27. S. H. Lee, P. Liu, H. M. Cheong, C. E. Tracy and S. K. Deb, *Solid State Ionics*, 2003, **165**, 217-221.
28. H. C. Jo, K. M. Kim, H. Cheong, S. H. Lee and S. K. Deb, *Electrochemical and Solid State Letters*, 2005, **8**, E39-E41.
29. R. Vellacheri, V. K. Pillai and S. Kurungot, *Nanoscale*, 2012, **4**, 890-896.
30. C. C. Hu, H. R. Chiang and C. C. Wang, *Journal of Solid State Electrochemistry*, 2003, **7**, 477-484.
31. P. Campbell, M. Ortner and C. Anderson, *Analytical Chemistry*, 1961, **33**, 58-61.
32. J. P. Zheng, *Electrochemical and Solid State Letters*, 1999, **2**, 359-361.